

Micromagnetic formalism for magnetic multipoles

Myoung-Woo Yoo¹ and Axel Hoffmann¹

¹*Department of Materials Science and Engineering and Materials Research Laboratory, The Grainger College of Engineering, University of Illinois Urbana Champaign, Illinois 61801, USA*

(Dated: January 14, 2025)

Cluster magnetic multipoles are order parameters that describe the symmetry of spin arrangements in magnetic materials. High-order multipoles are particularly important in non-collinear antiferromagnets, where they determine key physical properties such as the anomalous Hall effect and the magneto-optical Kerr effect. Although non-uniform multipole states have been observed at the micrometer scale, their mesoscopic properties remain largely unexplored. In this work, we develop a general micromagnetic formalism for cluster magnetic multipoles, enabling the study of the spin dynamics in non-uniform multipole systems. As an example, we apply this formalism to investigate magnetic-octupole domain-wall dynamics in the non-collinear antiferromagnet Mn_3Sn . Our results capture key features of domain-wall motion, including deformation and the emergence of effective inertial mass. This study provides a general framework for studying the dynamics of high-order cluster magnetic multipoles, which is essential for determining the mesoscopic physical properties of non-collinear magnetic materials.

I. INTRODUCTION

Antiferromagnets are a class of magnetic materials in which the arrangement of magnetic dipole moments results in nearly zero net magnetization. Due to their inherent magnetic stability and ultra-fast spin dynamics, antiferromagnetic materials have become essential in advanced spintronics for high-performance information technology applications [1–12].

Antiferromagnetic materials can have non-collinear spin configurations. Certain non-collinear antiferromagnets can exhibit large electrical and optical responses, such as anomalous Hall conductivity and magneto-optical Kerr effects, both strongly correlated with their spin structures [9, 13–17]. Notably, similar physical phenomena can arise from sharing equivalent symmetry characteristics [15, 18]. To clarify the link between symmetry and physical properties, the concept of cluster magnetic multipoles has been introduced, providing a powerful framework for understanding and harnessing antiferromagnets in spintronics [15, 18, 19].

One example, where such a multipole description of the antiferromagnetic spin structure has proven to be very useful is given by $D0_{19}$ -type non-collinear antiferromagnets, such as Mn_3Sn and Mn_3Ge , which possess a kagome crystal structure and an inverse-triangle spin configuration [14, 20–23]. These antiferromagnets host Weyl nodes near the Fermi level and a non-vanishing Berry curvature, resulting in pronounced macroscopic responses to external stimuli despite their negligible net magnetization [9, 24, 25]. In these antiferromagnets, the formation of Weyl nodes is closely associated with cluster magnetic multipole moments, thus their transport and optical properties can be modulated by controlling the octupole direction using magnetic fields and electric currents, analogous to manipulating magnetic dipoles in ferromagnets [14, 15, 21–23]. Electric switching of octupole moments, essential for antiferromagnetic spintronic devices, can be achieved through various mechanisms, including spin-orbit torque, spin-transfer torque, orbital torque, and thermal effects [10, 26–30]. Recently, domain-wall-mediated octupole switching has been reported, enabling more efficient octupole control [31].

Similar to magnetic dipole moments, cluster magnetic multipole moments can form non-uniform magnetic textures, such as magnetic-octupole domain walls and bubbles [25, 30–33]. Due to the distinctive octupole dynamics and complex anisotropies of non-collinear antiferromagnets, intricate dynamic behaviors of the magnetic textures are anticipated. The dynamics of octupole moments in non-collinear antiferromagnets differ from those of dipole moments, because their overall angular momentum is largely compensated [10, 33–36]. The octupole moments are mostly confined in the kagome plane and have a six-fold in-kagome-plane anisotropy. In addition, magnetic multipole domain walls can have non-trivial profiles due to their complex anisotropy [37].

Numerical simulations have been firmly established as powerful tools for studying complicate spin dynamics. Although analytical models can describe multipole domain-wall motion, numerical simulations become even more critical, especially for higher-dimensional or more complex multipole textures which hold potential for advanced spintronic applications [2, 31, 38–40]. While the atomistic-spin model can be used for numerical calculations, studying the dynamics of multipole textures in larger systems exceeding sub-micrometer scales is challenging due to limitations in computational power and memory [37, 40].

In ferromagnetic systems, micromagnetic models have been extensively used to overcome the limitation of numerical atomistic simulations [41–43]. This approach uses a representative magnetization for a finite volume and associated energy terms based on continuum theory, allowing for efficient computation with a good balance between detail and computational feasibility, even though some atomic-scale details are lost. This approach has also been extended to ferromagnets and collinear antiferromagnets, facilitating studies of mesoscopic domain structures, domain-wall motion, magnetization switching, and terahertz oscillations [44–46]. While several studies have explored octupole domain-wall motion, the comprehensive exploration of non-uniform octupole or higher-order multipole dynamics via micromagnetic methods remains largely unexplored [31, 40]. With recent demonstrations of domain-wall motion in non-collinear an-

tiferromagnets, investigating non-uniform magnetization dynamics on the micrometer scale has become both imperative and timely [31].

In this article, we develop a micromagnetic formalism for cluster magnetic multipoles to describe non-uniform multipole dynamics at the micrometer scale. From the general formalism, we establish a micromagnetic model for octupole magnetization in the non-collinear antiferromagnet, Mn_3Sn , and the corresponding energy terms which enable a micromagnetic approach for magnetic multipoles in antiferromagnets, analogous to the methods used in conventional micromagnetic models for ferromagnets. To validate the model, we simulate the dynamics of a single octupole magnetization and the octupole profiles of one-dimensional 60° domain walls. Building on this validation, we use the micromagnetic model to investigate phenomena beyond the reach of atomistic-spin simulations. We study the field-driven motion of 180° domain walls composed of three consecutive 60° domain walls. Our results reveal that domain-wall motion involves significant shape deformation which leads to inertial motion and an effective inertial mass. The results show that micromagnetic approach can capture key features of non-uniform magnetic multipole dynamics at the micrometer scale.

II. MICROMAGNETIC MODEL FOR MAGNETIC CLUSTER MULTIPOLES

We consider an antiferromagnet where the spin configuration in a unit cell remains largely preserved under moderate excitation. In this case, the arrangement of magnetic dipole moments can be described by a characteristic vector, \mathbf{c}_0 [15, 19]. Suppose there are n magnetic dipole moments located at sublattices $i = 1, \dots, n$ in a unit cell, and the positions are given by $\mathbf{r}_i = \mathbf{r}_0 + \Delta\mathbf{r}_i$, where \mathbf{r}_0 is the position of the unit cell and $\Delta\mathbf{r}_i$ is the relative position of sublattice i from \mathbf{r}_0 . If the dipole moments show collective motion relative to \mathbf{c}_0 , while maintaining the overall configuration, the magnetic moment at each sublattice, \mathbf{m}_i , can be described by \mathbf{c}_0 , *i.e.*,

$$\mathbf{m}_i = f_i(\mathbf{c}_0), \quad (1)$$

where f_i is a function that yields \mathbf{m}_i [Fig. 1(a)]. Therefore, the vector \mathbf{c}_0 defines the local antiferromagnetic multipole state of the unit cell and generally governs the transport and optical properties.

Consider a small volume V_c containing $N_{\text{u.c.}}$ unit cells. Within this volume, a representative characteristic vector, \mathbf{C}_0 , can be obtained by averaging the characteristic vectors over the volume [Fig. 1(b)]. The Lagrangian and the dissipative function density of \mathbf{C}_0 can be calculated as

$$\begin{aligned} L &= N_{\text{u.c.}} \sum_{i=1}^n \left\{ \frac{m_s}{\gamma} \dot{\varphi}_i \cos \theta_i - \epsilon_i \right\} \text{ and} \\ F &= N_{\text{u.c.}} \sum_{i=1}^n \left\{ \alpha \frac{m_s}{2\gamma} (\dot{\theta}_i^2 + \dot{\varphi}_i^2 \sin^2 \theta_i) \right\}, \end{aligned} \quad (2)$$

where φ_i and θ_i are the azimuthal and polar angles of the magnetic moment, $\mathbf{m}_i = (\sin \theta_i \cos \varphi_i, \sin \theta_i \sin \varphi_i, \cos \theta_i)$, obtained

from Eq. 1. m_s is the magnitude of an individual magnetic dipole moment, γ is the gyromagnetic ratio, and ϵ_i is the magnetic energy at each sublattice [47, 48].

Using Eq. 2, we obtain the equation of motion of \mathbf{C}_0 by solving the Euler-Lagrangian equation with respect to \mathbf{C}_0 . This equation serves as the counter part to the Landau-Lifshitz equation in the micromagnetic model for ferromagnets. Based on this equation of motion and associated micromagnetic energy terms, we can develop a micromagnetic model for magnetic multipoles.

As an illustrating example, we develop a micromagnetic model for the magnetic octupoles in Mn_3Sn . In a unit cell of Mn_3Sn , there are two kagome planes and six magnetic dipole moments, \mathbf{m}_i , where $i = 1, \dots, 6$ [see Fig. 1(a)]. The magnetic ground state can be obtained from the Hamiltonian,

$$\begin{aligned} \mathcal{H} &= -J_1 \sum_{\langle ij \rangle_z} \mathbf{m}_i \cdot \mathbf{m}_j - J_2 \sum_{\langle ij \rangle_{xy}} \mathbf{m}_i \cdot \mathbf{m}_j \\ &+ \sum_{\langle ij \rangle_{xy}} \mathbf{D} \cdot (\mathbf{m}_i \times \mathbf{m}_j) - \sum_i K (\hat{\mathbf{n}}_i \cdot \mathbf{m}_i)^2, \end{aligned} \quad (3)$$

where \mathbf{m}_i is a unit vector of magnetic dipole moments at each sublattice i [34]. J_1 and J_2 are isotropic exchange interaction constants between inter-plane and intra-plane nearest neighbor moments, respectively. A Dzyaloshinskii-Moriya interaction is included, specified by the vector $\mathbf{D} = D\hat{\mathbf{z}}$. K is the single-ion anisotropy constant and $\hat{\mathbf{n}}_i$ is the unit vector characterizing the local easy axis at position i . For simplicity, we do not consider thermal effects and any in-kagome-plane Dzyaloshinskii-Moriya interaction vectors in this model.

The ground state of Mn_3Sn is shown by arrows in Fig. 1(a). In this work, we used parameters $J_1 = J_2 = -2.803$ meV, $D = -0.635$ meV, $K = 0.187$ meV, and $m_s = 3\mu_B$, where μ_B is the Bohr magneton [34]. The magnetic dipole moments at the ground state form an anti-chiral triangular structure with approximately 120° angles in the kagome plane. Due to the local anisotropy, however, the dipole moments deviate slightly from the 120° angle by $\delta\varphi_i$ which generates a net magnetization along the octupole vector, M_{oct} .

As shown in Eq. 1, the magnetic dipole vectors, $\mathbf{m}_i = (\sin \theta_i \cos \varphi_i, \sin \theta_i \sin \varphi_i, \cos \theta_i)$, can be described by the magnetic octupole vector, $\mathbf{m}_{\text{oct}} = (\sin \theta_{\text{oct}} \cos \varphi_{\text{oct}}, \sin \theta_{\text{oct}} \sin \varphi_{\text{oct}}, \cos \theta_{\text{oct}})$ as

$$\begin{aligned} \varphi_1 &= -\varphi_{\text{oct}} + \frac{\pi}{3} + \delta\varphi_1 \\ \varphi_2 &= -\varphi_{\text{oct}} + \pi + \delta\varphi_2 \\ \varphi_3 &= -\varphi_{\text{oct}} + \frac{5\pi}{3} + \delta\varphi_3 \\ \varphi_4 &= -\varphi_{\text{oct}} + \frac{\pi}{3} + \delta\varphi_4 \\ \varphi_5 &= -\varphi_{\text{oct}} + \pi + \delta\varphi_5 \\ \varphi_6 &= -\varphi_{\text{oct}} + \frac{5\pi}{3} + \delta\varphi_6, \end{aligned} \quad (4)$$

and

$$\theta_1 = \theta_2 = \theta_3 = \theta_4 = \theta_5 = \theta_6 = \theta_{\text{oct}} = \frac{\pi}{2}, \quad (5)$$

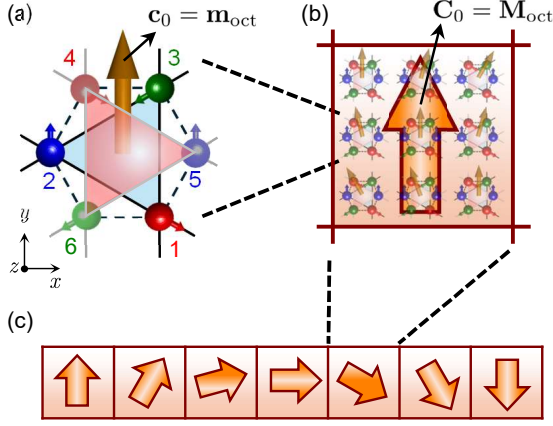


Figure 1. Micromagnetic model for non-collinear antiferromagnets. (a) Representative magnetic ground state in a magnetic unit cell numerically calculated using an atomistic-spin model. The spheres and arrows represent Mn atoms and their magnetic moments, while the vivid blue and dim red planes indicate different planes. The numbers correspond to the sublattice indices. Solid and dashed lines represent isotropic exchange interactions between intra-plane and inter-plane nearest-neighbor atoms, respectively. The large orange arrow at the center denotes the octupole vector $\mathbf{c}_0 = \mathbf{m}_{\text{oct}}$ defined by Eq. 4. (b) A finite volume where there are sufficiently many number of magnetic unit cells. The spatial variations of the octupole vector is small. The large orange arrow shows the average octupole magnetization, $\mathbf{C}_0 = \mathbf{M}_{\text{oct}}$, over the volume. (c) A non-uniform magnetic configuration represented by \mathbf{M}_{oct} whose dynamics can be calculated by Eq. 6.

where $\delta\varphi_i$ is a deviation angle of the magnetic dipole moments from 120° due to the local anisotropy. At the ground state, $\delta_{1,0} = \delta_{4,0} = -\delta_{2,0} = -\delta_{5,0}$ and $\delta_{3,0} = \delta_{6,0} = 0$. Note that we define the octupole vector parallel to the direction of the net magnetic moment.

Consider a finite volume, V_c , in a non-uniform Mn_3Sn medium containing a sufficient number of Mn_3Sn unit cells. By assuming the octupole vectors in V_c as being mostly uniform, we obtain an octupole magnetization vector $\mathbf{M}_{\text{oct}} = M_{\text{oct}}(\sin \Theta_{\text{oct}} \cos \Phi_{\text{oct}}, \sin \Theta_{\text{oct}} \sin \Phi_{\text{oct}}, \cos \Theta_{\text{oct}})$ by averaging the octupole vectors over V_c . From Eqs. 2 and 4, we derive the Lagrangian and the dissipative function densities of the octupole magnetization vector [49]. By solving the Euler-Lagrangian equation, we obtain the equation of motion of the octupole magnetization, \mathbf{M}_{oct} , in V_c ,

$$\begin{aligned} \dot{\Phi}_{\text{oct}} &= 0 \quad \text{and} \\ \dot{\Phi}_{\text{oct}} &= -\frac{\gamma}{\alpha M_{\text{Mn}} V_c} \frac{\partial E_{\text{tot}}}{\partial \Phi_{\text{oct}}} - \frac{\gamma \theta_{\text{sh}} p_z \hbar}{\alpha 2 M_{\text{Mn}} e d} j_{\text{hm}}, \end{aligned} \quad (6)$$

where j_{hm} is the current density in the adjacent heavy-metal layer, θ_{sh} is the spin-Hall angle, p_z is the spin polarization in the z -direction, d is the thickness of an antiferromagnet layer, and M_{Mn} is the magnetization of Mn in Mn_3Sn . Note that the second term of $\dot{\Phi}_{\text{oct}}$ represents the spin-orbit torque calculated from the corresponding dissipative function density [see Supplementary Material] [49]. Equation 6 is fundamentally identical with the equation of motion of a single octupole mo-

ment of a magnetic unit cell [34, 36].

Next, we calculate the micromagnetic energy terms. The total magnetic energy of the volume, E_{tot} , is given by $E_{\text{tot}} = E_{\text{ext}} + E_{\text{ani}} + E_{\text{exc}}$, where E_{exc} , E_{ani} , E_{ext} are the Zeeman, exchange, and anisotropy energies, respectively. The Dzyaloshinskii–Moriya interaction energy is included in E_{exc} , and we do not consider the demagnetization energy due to the negligible net magnetization. The Zeeman and anisotropy energies can be calculated by summing the energies of individual octupole moments. For the exchange energy, we consider all connections between dipole moments of a unit cell [see Supplementary Materials]. The micromagnetic energies are given by,

$$\begin{aligned} \frac{E_{\text{ext}}}{V_c} &= -\mu_0 M_{\text{oct}} H \cos \Delta\Phi, \\ \frac{E_{\text{exc}}}{V_c} &= A_{\text{ex},x} \left(\frac{\partial \Phi_{\text{oct}}}{\partial x} \right)^2 + A_{\text{ex},y} \left(\frac{\partial \Phi_{\text{oct}}}{\partial y} \right)^2 + A_{\text{ex},z} \left(\frac{\partial \Phi_{\text{oct}}}{\partial z} \right)^2, \quad (7) \\ \frac{E_{\text{ani}}}{V_c} &= K_6 \cos^2 3\Phi_{\text{oct}}. \end{aligned}$$

Note that we assume that the octupole vectors lie in the kagome plane with negligible out-of-kagome-plane components, thus only the azimuthal angle, Φ_{oct} is considered. M_{oct} is an octupole magnetization magnitude at the ground state, $\Delta\Phi$ is the angular difference between the external field and the octupole magnetization. The octupole magnetization exhibits a six-fold anisotropy with a magnitude of K_6 . Mn_3Sn films can have a two-fold perpendicular magnetic anisotropy due to in-plane tensile strain [33, 36, 50]. In that case E_{ani} in Eq. 7 can include an additional $K_2 \cos^2 \Phi_{\text{oct}}$ term. Numerically, we obtained $M_{\text{oct}} = 6.1 \times 10^3 \text{ Am}^{-1}$ and $K_6 = 37.5 \text{ Jm}^{-3}$. Although these values can be calculated analytically, we use the numerically obtained values in this work [see Supplementary Material] [34].

$A_{\text{ex},x}$, $A_{\text{ex},y}$, and $A_{\text{ex},z}$ are the coefficients for the exchange interaction in the x -, y -, and z -directions, respectively. They can be calculated by

$$\begin{aligned} A_{\text{ex},x} &= A_{\text{ex},y} = -\left(\frac{J_1 + 3J_2 + 3D\sqrt{3}}{8\sqrt{2}a_0} \right) \quad \text{and} \\ A_{\text{ex},y} &= -\frac{J_1}{2\sqrt{2}a_0}, \end{aligned} \quad (8)$$

respectively, where a_0 is the distance between nearest sublattices, $\sim 0.28 \text{ nm}$. In our calculation, $A_{\text{ex},x} = A_{\text{ex},y} = 7.3 \times 10^{-13} \text{ Jm}^{-1}$, and $A_{\text{ex},z} = 5.6 \times 10^{-13} \text{ Jm}^{-1}$. Equation 8 can be modified if additional exchange connections are considered [34, 51].

RESULTS

Single Octupole Magnetization Dynamics

We numerically calculated the dynamics of a single octupole magnetization using the micromagnetic model.

In the first simulation, we focused on the field-driven octupole dynamics. Initially, the octupole was oriented in the $+y$ -direction, and a magnetic field was applied parallel to the $+x$ -direction to induce the octupole motion. The volume of the cell was $10 \times 10 \times 10 \text{ nm}^3$, and periodic boundary conditions were applied in the x -, y -, and z -directions. We obtained the time evolution of the octupole angle, Φ_{oct} , as well as the change in total magnetic energy, ΔE_{tot} , by solving Eqs. 6 and 7 with the Runge-Kutta method. The results are plotted in Fig. 2(a). When a small magnetic field, $\mu_0 H_x = 10 \text{ mT}$, is applied, the octupole remains near $\Phi_{\text{oct}} = 90^\circ$, because the octupole could not overcome the energy barrier. However, when a larger magnetic field, $\mu_0 H_x = 30$ or 50 mT , is applied, the octupole exhibits rotational motion, and stabilize near the other ground state at $\Phi_{\text{oct}} = 30^\circ$. During the motion, ΔE_{tot} also decreases due to the reduction in the Zeeman energy. We also conducted the same simulation using the atomistic-spin model as shown in Fig. 2(b), and obtained nearly identical results.

In the second simulation, we numerically calculated the octupole rotation induced by the spin-orbit torque at a current density, j_{hm} , in an adjacent heavy-metal layer. For this simulation, we used a spin-Hall angle of $\theta_{\text{sh}} = 0.1$ and a Mn_3Sn film thickness of $d = 40 \text{ nm}$. The applied spin polarization, \mathbf{p} , was parallel to the $+z$ -direction. The calculation results are shown in Fig. 2(c). If j_{hm} is larger than the critical value, $j_{\text{hm}} = 0.2$ and 0.3 TAm^{-2} , the octupole begins rotating continuously, and ΔE_{tot} oscillates due to the six-fold anisotropy, while the magnetization does not show any rotation motion, when $j_{\text{hm}} = 0.1 \text{ TAm}^{-2}$. We also obtained a similar behavior from the atomistic-spin model as depicted in Fig. 2(d). Note that the atomistic-spin model shows a slight initial increase in ΔE_{tot} due to small spin rearrangement caused by the spin-orbit torque, but, after 0.05 ns , ΔE_{tot} exhibits almost the same dynamics closely matched those of the micromagnetic model.

The consistency between the results from the micromagnetic and the atomistic-spin models, as shown in Fig. 2 confirms the agreement between the two models with respect to the octupole dynamics.

60-degree Domain Walls

We investigated non-uniform octupole configuration, one-dimensional magnetic domain walls. In Mn_3Sn , the domain walls can show some different features that those in conventional ferromagnets. First, the kagome plane direction determines the types of domain walls due to the strong in-plane anisotropy [31]. For example, the Néel-type walls form when the domain-wall propagation direction is along the x - or y -directions, while the Bloch-type walls appear when the propagation is along the z -direction. [see Fig. 3(a)]. In addition, a 180° domain wall in Mn_3Sn can have a staircase-like structure consisting of three 60° domain walls due to the six-fold anisotropy [37]. In this study, we numerically calculated the octupole profile of the 60° domain wall, where Φ_{oct} varies from $+90^\circ$ to $+30^\circ$. Hereafter, we will refer to this domain wall as a $+90^\circ \leftrightarrow +30^\circ$ domain wall.

The profiles of the Néel- and Bloch-types domain walls

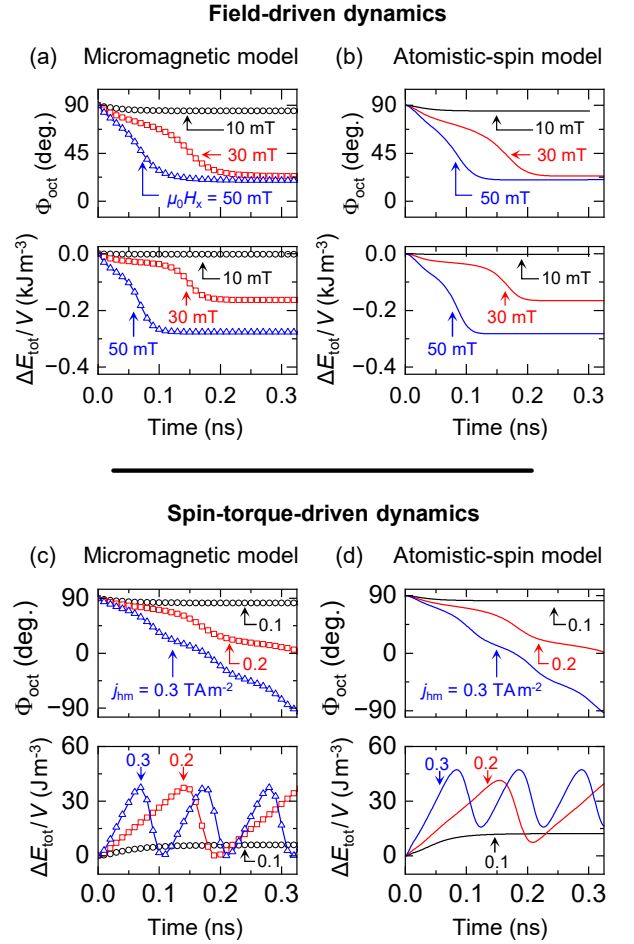


Figure 2. Comparison between the micromagnetic model and the atomistic-spin model based numerical simulations for an octupole magnetization dynamics (a) Time evolution of the octupole angle, Φ_{oct} , (top) and the total magnetic energy, ΔE_{tot} , (bottom) calculated using the micromagnetic model under different $+x$ -directional magnetic fields, H_x . ΔE_{tot} is normalized by the system volume, V . (b) Same as (a), but calculated using the atomistic-spin model. (c) Φ_{oct} and ΔE_{tot} calculated using the micromagnetic model under the spin-orbit torque at a current density, j_{hm} , in an adjacent heavy-metal layer. The applied spin polarization, \mathbf{p} is in the $+z$ -direction. (d) Same as (c), but obtained using the atomistic-spin model.

are plotted in Figs. 3(b) and 3(c) (symbols), respectively, which are numerically calculated using the micromagnetic model. We additionally plotted the profiles simulated by the atomistic-spin model in Fig. 3(b) (solid lines), which closely match the results obtained from the micromagnetic model.

The 60° -domain-wall profiles in Mn_3Sn can be expressed analytically as $\Phi_{\text{oct}} = -(1/3) \arctan\{\sinh(\pi x/\delta_w)\} + \pi/3$, where δ_w is the domain-wall width, $\delta_w = (\pi \sqrt{A_{zx}})/(3 \sqrt{K_6})$ [see Supplementary Material]. In our system, $\delta_w = 145 \text{ nm}$ and 128 nm for the Néel- and Bloch-type domain walls, respectively. Therefore, the domain-wall profiles for the Néel- and Bloch-type domain walls show a slight difference as shown in Fig. 3(d). These results clearly demonstrate that the micromagnetic model can accurately describe the non-uniform

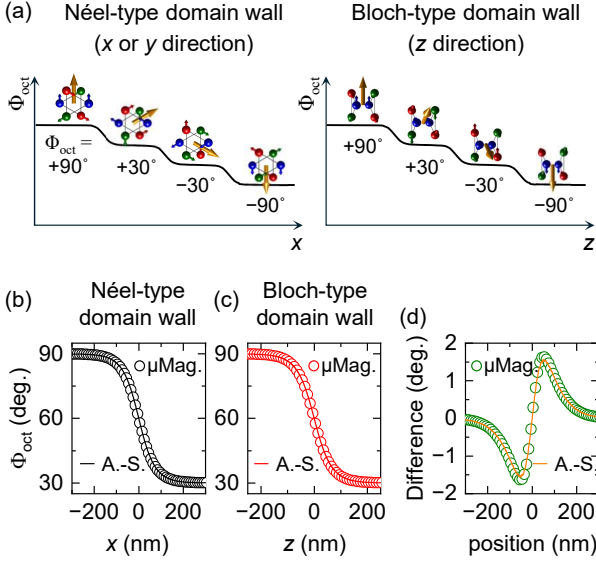


Figure 3. Profiles of domain walls in Mn_3Sn . (a) Schematic representations of the Néel-type (left) and Bloch-type (right) domain walls propagating along the x - and z -directions, respectively. The orange arrows indicate the orientation of octupole vectors. A 180° domain wall consists of three consecutive 60° domain walls. (b) Octupole-angle profile, Φ_{oct} , for a Néel-type 60° domain wall along the x -direction, calculated by both the micromagnetic model (symbols) and the atomistic-spin model (solid line) numerically. (c) Same as (b), but for the Bloch-type domain wall along the z -direction. (d) Difference in Φ_{oct} between (b) and (c), calculated using the micromagnetic model (symbols) and the atomistic-spin model (solid line).

octupole configurations.

Next, we calculated the domain-wall motion by applying a magnetic field, H_y , and determined the domain-wall velocities. Once the field is applied, the domain wall begins to move with a finite velocity. The domain-wall motion involves shape deformation due to changes in the octupole angles of two domains, $\Phi_{\text{oct}} = +30^\circ$ and -30° . In Figs. 4(a)-4(c), we show the domain-wall profiles for three 60° domain walls, both at rest (solid lines) and during the stationary motion (dashed lines) calculated using the micromagnetic model. Note that we were unable to calculate the domain-wall motion with the atomistic-spin model, because of computational resource limitations.

The time evolution of the domain-wall position and the velocities are plotted in Figs. 4(d)- 4(f) and Fig. 4(g), respectively. The velocity increases monotonically with increasing H_y for all domain walls, but the velocities differ for each domain wall. The $30^\circ \leftrightarrow -30^\circ$ domain wall moves at roughly twice the speed of the others. At lower fields, $\mu_0 H_y < 7$ mT, the velocities of the $+90^\circ \leftrightarrow +60^\circ$ and $-30^\circ \leftrightarrow -90^\circ$ domain walls are nearly identical, but the former becomes slightly faster at higher fields, $\mu_0 H_y \leq 7$ mT. These results imply that the 180° domain wall in Mn_3Sn can show complex deformation during the field-driven motion due to the different velocities, and this is difficult to predict using a simplified analytic model.

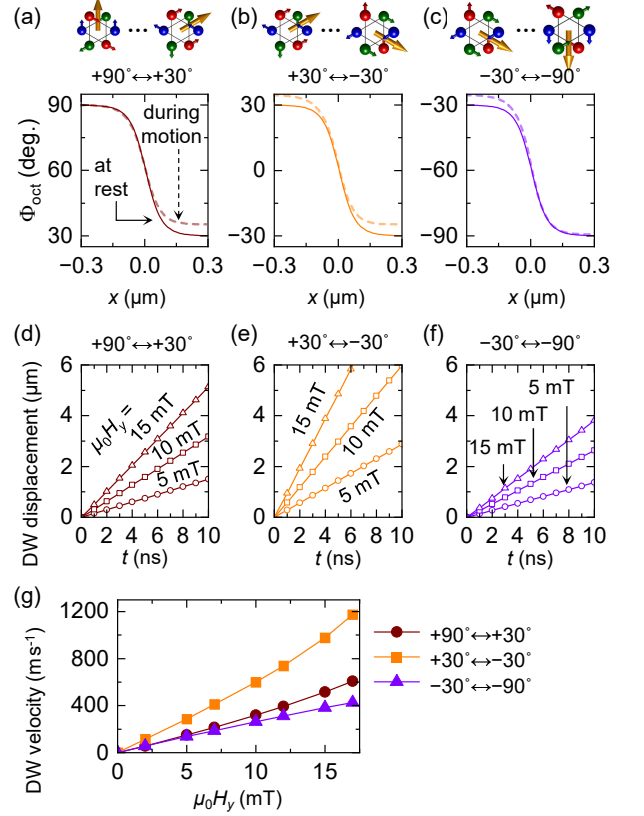


Figure 4. Domain-wall (DW) motion of 60° domain walls. (a)-(c) The octupole-angle profiles, Φ_{oct} , at rest (solid lines) and during motion (dashed lines) under $\mu_0 H_y = 10$ mT for the $+90^\circ \leftrightarrow +30^\circ$, $+30^\circ \leftrightarrow -30^\circ$, and $-30^\circ \leftrightarrow -90^\circ$ domain walls, respectively. (d)-(f) Time evolution of the domain-wall positions under different H_y for the three 60° domain walls. (g) Velocities of the 60° domain walls as a function of H_y .

180-degree Domain Walls

We calculated the profile and motion of a 180° domain wall using the micromagnetic model. Due to the six-fold symmetric anisotropy in Mn_3Sn , the 180° domain wall has a staircase-like structure, composed of three 60° domain walls [37]. Note that, without considering the magnetostatic energy, there is no optimized distance between the 60° domain walls. To address this in our simulation, we introduced an additional uniaxial anisotropy in the y -direction, i.e., $E_{\text{ani}} = V_c \{K_6 \cos^2 3\Phi_{\text{oct}} + K_2 \cos^2 \Phi_{\text{oct}}\}$. In this calculation, we used $K_u = 10 \text{ Jm}^{-3}$ which is about 30% of $K_6 = 37.5 \text{ Jm}^{-3}$. It has been reported that such uniaxial anisotropy can be introduced by in-plane tensile strain in Mn_3Sn [33, 36, 50].

In Fig. 5(a), we show the calculated Φ_{oct} profile of a 180° Néel-type domain wall. The slopes and shapes of each step is in good agreements with the individual 60° domain walls as shown by colored lines in Fig. 5(a). Note that the total width of the 180° domain wall decreases with increasing K_u [see Supplemental Material].

Next, we induced motion of the 180° domain wall by ap-

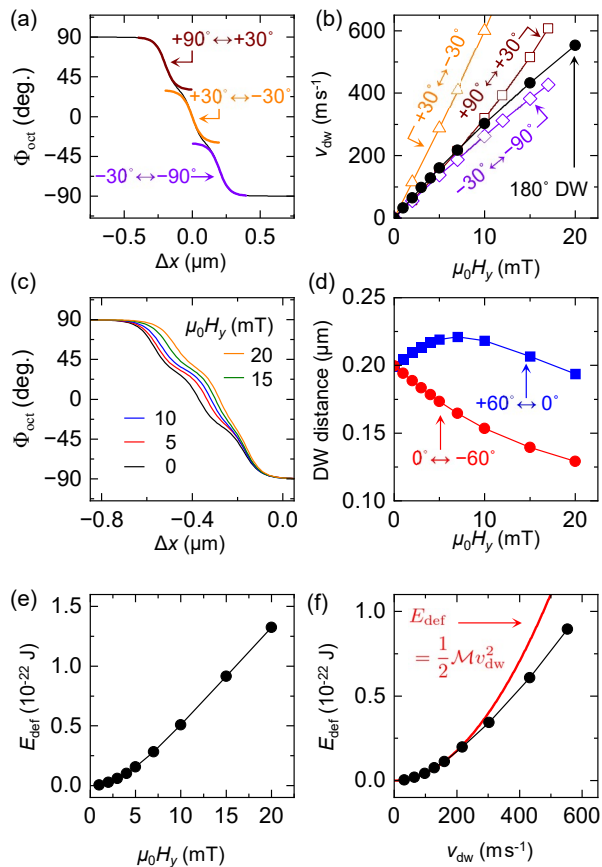


Figure 5. 180° domain-wall profile and dynamics. (a) The 180° domain-wall calculated using the micromagnetic model (black curve). To stabilize the domain wall, an additional effective uniaxial anisotropy was included in the calculation. The brown, orange and violet curves represent three 60° domain walls identical to Figs. 4(a)-(c), calculated without the effective uniaxial anisotropy. (b) Domain-wall velocity, v_{dw} , of 180° (black closed circle), 90° \leftrightarrow 30° (brown open square), 30° \leftrightarrow -30° (orange open triangle), and -30° \leftrightarrow -90° (violet open diamond) at steady state under H_y . (c) 180° domain-wall profiles during steady-state motion under different $\mu_0 H_y$. (d) Deformation energy of a domain wall, E_{def} during steady-state motion as a function of H_y . (e) E_{def} as a function of the domain-wall velocity, v_{dw} (black circle and line). The red line shows a quadratic fit for low v_{dw} . \mathcal{M} is the effective inertial mass of the domain wall for low v_{dw} .

plying a magnetic field in the $+y$ -direction, H_y . As shown in Fig. 5(b) (black closed circle), the domain-wall velocity, v_{dw} , increases with increasing H_y , but the slope decreases slightly similar to the -30° \leftrightarrow -90° domain wall shown in Fig. 4(g). v_{dw} of the 180° domain wall is faster than that of the -30° \leftrightarrow -90° domain wall, but slower than both the +90° \leftrightarrow +30° and the -30° \leftrightarrow -90° domain walls. This result shows that the 180°-domain-wall motion is not determined by one of the 60° domain walls, and results from complex interaction among the three 60° domain walls. We also obtained the relation between v_{dw} and H_y for the z -directional Bloch domain wall as provided in the Supplementary Material.

Because the different 60° domain walls exhibit different velocities while being driven by H_y , the shape of the 180°

domain wall deforms under H_y . In Fig. 5(c), we show the Φ_{oct} profile during steady-state motion for different values of H_y . At the ground state, *i.e.*, $H_y = 0$ mT, the three domain walls are evenly spaced. However, during motion, the total width of the domain wall decreases. In particular, the distance between +30° \leftrightarrow -30° and -30° \leftrightarrow -90° domain walls decreases as H_y increases. To clarify this deformation, we plotted the distances between the domain-wall centers, *i.e.*, 60°, 0°, and -60°, in Fig. 5(d) as a function of H_y . When $H_y \leq 7$ mT, the distances between 0° and -60° positions and +60° and 0° positions monotonically decreases and increases with increasing H_y , due to different velocity of the domain walls. However, the distance between +60° and 0° begins to decrease from $H_y \approx 7$ mT, to reduce the anisotropy energy.

Deformation during the motion increases the energy of the domain wall, as shown in Fig. 5(e) similar to the ferromagnetic domain walls [52]. In ferromagnets, the domain-wall angle changes with increasing v_{dw} and the deformation increases the domain-wall energy, E_{def} . When v_{dw} is slow, $E_{def} \propto v_{dw}^2$ approximately, and an effective inertial mass of the domain wall is defined as $\mathcal{M} = 2E_{def}/v_{dw}^2$.

To obtain an effective inertial mass, \mathcal{M} , of the 180° domain wall in Mn_3Sn , we plotted the deformation energy as a function of the domain-wall velocity, v_{dw} , in Fig. 5(f). The relation shows a quadratic form at low v_{dw} , and we obtained $\mathcal{M} \approx 8.8 \times 10^{-28}$ kg. Additionally we calculated the mass of the Bloch domain wall, which has a value about twice as large, $\mathcal{M} \approx 1.7 \times 10^{-27}$ kg [see Supplementary Material]. Note that the mass per the cross-sectional area for the Néel and Bloch domain walls are 8.8×10^{-12} and 1.7×10^{-11} kg m^{-2} which have the same order with the mass density of a ferromagnetic domain wall in Permalloy, 3×10^{-11} kg m^{-2} , reported in Ref. [53]. The inertial mass of the antiferromagnetic domain walls suggests that it could exhibit inertial motion of the antiferromagnetic domain wall [see Supplementary Material], and the inertial mass should be experimentally measurable, similar to what has been observed in ferromagnetic systems [53–55].

III. CONCLUSION

In this article, we developed a micromagnetic formalism for magnetic multipoles and investigated non-uniform multipole dynamics at the micrometer scale. By introducing a characteristic vector within a unit cell to represent the multipole states, we can derive the equation of motion for the vector and obtain the associated micromagnetic energy terms even though some atomic-scale details are lost. This formalism enables micromagnetic approaches for multipole antiferromagnets analogous to those used in conventional micromagnetic models for ferromagnets. As a demonstration, we numerically investigated the octupole domain-wall dynamics in the non-collinear antiferromagnet Mn_3Sn using this micromagnetic framework. The model successfully captured the key features of both 60° and 180° domain walls. The simulations revealed that field-driven domain-wall motion induces profile deformations, resulting in additional magnetic energy increase during motion. From the increase in deformation-induced domain-wall en-

ergy, we quantified the effective inertial mass of the domain wall in non-collinear antiferromagnets. This study establishes a general framework for exploring the dynamics of high-order magnetic multipoles at the micrometer scale, which is crucial for understanding the mesoscopic physical properties of magnetic materials.

ACKNOWLEDGMENTS

This research is supported by the NSF through the University of Illinois Urbana-Champaign Materials Research Science and Engineering Center Grant No. DMR-1720633 and is carried out in part in the Materials Research Laboratory Central Research Facilities, University of Illinois.

-
- [1] T. Jungwirth, X. Marti, P. Wadley, and J. Wunderlich, *Nature Nanotechnology* **11**, 231 (2016).
- [2] V. Baltz, A. Manchon, M. Tsoi, T. Moriyama, T. Ono, and Y. Tserkovnyak, *Reviews of Modern Physics* **90**, 015005 (2018).
- [3] S. A. Siddiqui, J. Sklenar, K. Kang, M. J. Gilbert, A. Schleife, N. Mason, and A. Hoffmann, *Journal of Applied Physics* **128**, 040904 (2020).
- [4] Y. Cheng, S. Yu, M. Zhu, J. Hwang, and F. Yang, *Physical Review Letters* **124**, 027202 (2020).
- [5] S. Y. Bodnar, L. Šmejkal, I. Turek, T. Jungwirth, O. Gomonay, J. Sinova, A. A. Sapozhnik, H.-J. Elmers, M. Kläui, and M. Jourdan, *Nature Communications* **9**, 348 (2018).
- [6] T. Matalla-Wagner, M.-F. Rath, D. Graulich, J.-M. Schmalhorst, G. Reiss, and M. Meinert, *Physical Review Applied* **12**, 064003 (2019).
- [7] M. Grzybowski, P. Wadley, K. Edmonds, R. Beardsley, V. Hills, R. Champion, B. Gallagher, J. Chauhan, V. Novak, T. Jungwirth, F. Maccherozzi, and S. Dhesi, *Physical Review Letters* **118**, 057701 (2017).
- [8] P. Wadley, B. Howells, J. Železný, C. Andrews, V. Hills, R. P. Champion, V. Novák, K. Olejník, F. Maccherozzi, S. S. Dhesi, S. Y. Martin, T. Wagner, J. Wunderlich, F. Freimuth, Y. Mokrousov, J. Kuneš, J. S. Chauhan, M. J. Grzybowski, A. W. Rushforth, K. W. Edmonds, B. L. Gallagher, and T. Jungwirth, *Science* **351**, 587 (2016).
- [9] S. Nakatsuji, N. Kiyohara, and T. Higo, *Nature* **527**, 212 (2015).
- [10] H. Tsai, T. Higo, K. Kondou, T. Nomoto, A. Sakai, A. Kobayashi, T. Nakano, K. Yakushiji, R. Arita, S. Miwa, Y. Otani, and S. Nakatsuji, *Nature* **580**, 608 (2020).
- [11] L. Han, X. Fu, R. Peng, X. Cheng, J. Dai, L. Liu, Y. Li, Y. Zhang, W. Zhu, H. Bai, Y. Zhou, S. Liang, C. Chen, Q. Wang, X. Chen, L. Yang, Y. Zhang, C. Song, J. Liu, and F. Pan, *Science Advances* **10**, eadn0479 (2024).
- [12] M. Meinert, D. Graulich, and T. Matalla-Wagner, *Physical Review Applied* **9**, 064040 (2018).
- [13] T. Tomizawa and H. Kontani, *Physical Review B* **80**, 100401 (2009).
- [14] H. Chen, Q. Niu, and A. H. MacDonald, *Physical Review Letters* **112**, 017205 (2014).
- [15] M.-T. Suzuki, T. Koretsune, M. Ochi, and R. Arita, *Physical Review B* **95**, 094406 (2017).
- [16] H. Chen, T.-C. Wang, D. Xiao, G.-Y. Guo, Q. Niu, and A. H. MacDonald, *Physical Review B* **101**, 104418 (2020).
- [17] R. Shindou and N. Nagaosa, *Physical Review Letters* **87**, 116801 (2001).
- [18] S. Hayami, *Symmetry* **16**, 926 (2024).
- [19] R. Winkler and U. Zülicke, *Physical Review B* **107**, 155201 (2023).
- [20] E. Krén, J. Paitz, G. Zimmer, and E. Zsoldos, *Physica B+C* **80**, 226 (1975).
- [21] S. Tomiyoshi and Y. Yamaguchi, *Journal of the Physical Society of Japan* **51**, 2478 (1982).
- [22] P. J. Brown, V. Nunez, F. Tasset, J. B. Forsyth, and P. Radhakrishna, *Journal of Physics: Condensed Matter* **2**, 9409 (1990).
- [23] J. Kübler and C. Felser, *EPL (Europhysics Letters)* **108**, 67001 (2014).
- [24] M. Ikhlas, T. Tomita, T. Koretsune, M.-T. Suzuki, D. Nishio-Hamane, R. Arita, Y. Otani, and S. Nakatsuji, *Nature Physics* **13**, 1085 (2017).
- [25] T. Higo, H. Man, D. B. Gopman, L. Wu, T. Koretsune, O. M. J. van 't Erve, Y. P. Kabanov, D. Rees, Y. Li, M.-T. Suzuki, S. Patankar, M. Ikhlas, C. L. Chien, R. Arita, R. D. Shull, J. Orenstein, and S. Nakatsuji, *Nature Photonics* **12**, 73 (2018).
- [26] H. Xie, X. Chen, Q. Zhang, Z. Mu, X. Zhang, B. Yan, and Y. Wu, *Nature Communications* **13**, 5744 (2022).
- [27] H. Xie, N. Zhang, Y. Ma, X. Chen, L. Ke, and Y. Wu, *Nano Letters* **23**, 10274 (2023).
- [28] G. K. Krishnaswamy, G. Sala, B. Jacot, C.-H. Lambert, R. Schlitz, M. D. Rossell, P. Noël, and P. Gambardella, *Physical Review Applied* **18**, 024064 (2022).
- [29] B. Pal, B. K. Hazra, B. Göbel, J.-C. Jeon, A. K. Pandeya, A. Chakraborty, O. Busch, A. K. Srivastava, H. Deniz, J. M. Taylor, H. Meyerheim, I. Mertig, S.-H. Yang, and S. S. P. Parkin, *Science Advances* **8**, eabo5930 (2022).
- [30] M.-W. Yoo, V. O. Lorenz, A. Hoffmann, and D. G. Cahill, *APL Materials* **12**, 081107 (2024).
- [31] M. Wu, T. Chen, T. Nomoto, Y. Tserkovnyak, H. Isshiki, Y. Nakatani, T. Higo, T. Tomita, K. Kondou, R. Arita, S. Nakatsuji, and Y. Otani, *Nature Communications* **15**, 4305 (2024).
- [32] T. Uchimura, J.-Y. Yoon, Y. Sato, Y. Takeuchi, S. Kanai, R. Takechi, K. Kishi, Y. Yamane, S. DuttaGupta, J. Ieda, H. Ohno, and S. Fukami, *Applied Physics Letters* **120**, 172405 (2022).
- [33] T. Higo, K. Kondou, T. Nomoto, M. Shiga, S. Sakamoto, X. Chen, D. Nishio-Hamane, R. Arita, Y. Otani, S. Miwa, and S. Nakatsuji, *Nature* **607**, 474 (2022).
- [34] J. Liu and L. Balents, *Physical Review Letters* **119**, 087202 (2017).
- [35] Y. Takeuchi, Y. Yamane, J.-Y. Yoon, R. Itoh, B. Jinnai, S. Kanai, J. Ieda, S. Fukami, and H. Ohno, *Nature Materials* **20**, 1364 (2021).
- [36] J.-Y. Yoon, P. Zhang, C.-T. Chou, Y. Takeuchi, T. Uchimura, J. T. Hou, J. Han, S. Kanai, H. Ohno, S. Fukami, and L. Liu, *Nature Materials* **10.1038/s41563-023-01620-2** (2023).
- [37] S. Sugimoto, Y. Nakatani, Y. Yamane, M. Ikhlas, K. Kondou, M. Kimata, T. Tomita, S. Nakatsuji, and Y. Otani, *Communications Physics* **3**, 111 (2020).
- [38] X. Zhang, Y. Zhou, and M. Ezawa, *Scientific Reports* **6**, 24795 (2016).
- [39] X. Li, C. Collignon, L. Xu, H. Zuo, A. Cavanna, U. Gennser, D. Mailly, B. Fauqué, L. Balents, Z. Zhu, and K. Behnia, *Nature Communications* **10**, 3021 (2019).

- [40] Y. Yamane, O. Gomonay, and J. Sinova, *Physical Review B* **100**, 054415 (2019).
- [41] W. F. Brown, *Micromagnetics*, Interscience tracts on physics and astronomy (Interscience Publishers, New York, 1963).
- [42] J. Fidler and T. Schrefl, *Journal of Physics D: Applied Physics* **33**, R135 (2000).
- [43] C. Abert, *The European Physical Journal B* **92**, 120 (2019).
- [44] V. Puliafito, R. Khymyn, M. Carpentieri, B. Azzarboni, V. Tiberkevich, A. Slavin, and G. Finocchio, *Physical Review B* **99**, 024405 (2019).
- [45] U. Atxitia, P. Nieves, and O. Chubykalo-Fesenko, *Physical Review B* **86**, 104414 (2012).
- [46] D. Suess, T. Schrefl, W. Scholz, J.-V. Kim, R. Stamps, and J. Fidler, *IEEE Transactions on Magnetics* **38**, 2397 (2002).
- [47] W. Döring, *Zeitschrift für Naturforschung A* **3**, 373 (1948).
- [48] M. D. Stiles and J. Miltat, *Spin Dynamics in Confined Magnetic Structures III*, edited by Hillebrands and Thiaville, Topics in Applied Physics, Vol. Volume 101/2006 (Springer Berlin / Heidelberg, 2006).
- [49] G. Consolo, G. Gubbiotti, L. Giovannini, and R. Zivieri, *Applied Mathematics and Computation* **217**, 8204 (2011).
- [50] M. Ikhlas, S. Dasgupta, F. Theuss, T. Higo, S. Kittaka, B. J. Ramshaw, O. Tchernyshyov, C. W. Hicks, and S. Nakatsuji, *Nature Physics* [10.1038/s41567-022-01645-5](https://doi.org/10.1038/s41567-022-01645-5) (2022).
- [51] P. Park, J. Oh, K. Uhlířová, J. Jackson, A. Deák, L. Szunyogh, K. H. Lee, H. Cho, H.-L. Kim, H. C. Walker, D. Adroja, V. Sechovský, and J.-G. Park, *npj Quantum Materials* **3**, 63 (2018).
- [52] B. Hillebrands and A. Thiaville, *Spin dynamics in confined magnetic structures III*, Topics in applied physics, v. 101 (Springer, Berlin ;, 2006).
- [53] J. Rhensius, L. Heyne, D. Backes, S. Krzyk, L. J. Heyderman, L. Joly, F. Nolting, and M. Kläui, *Physical Review Letters* **104**, 067201 (2010).
- [54] E. Saitoh, H. Miyajima, T. Yamaoka, and G. Tatara, *Nature* **432**, 203 (2004).
- [55] F. Büttner, C. Moutafis, M. Schneider, B. Krüger, C. M. Günther, J. Geilhufe, C. Schmising, J. Mohanty, B. Pfau, S. Schaffert, A. Bisig, M. Foerster, T. Schulz, C. Vaz, J. H. Franken, H. J. M. Swagten, M. Kläui, and S. Eisebitt, *Nature Physics* **11**, 225 (2015).

Supplementary Material for “Micromagnetic formalism for magnetic multipoles”

Myoung-Woo Yoo¹ and Axel Hoffmann¹

¹*Department of Materials Science and Engineering and Materials Research Laboratory, The Grainger College of Engineering, University of Illinois Urbana Champaign, Illinois 61801, USA*

arXiv:2501.07513v1 [cond-mat.mes-hall] 13 Jan 2025

EQUATION OF MOTION OF A OCTUPOLE MAGNETIZATION IN Mn_3Sn

Here we calculate equation of motion for Mn_3Sn . We describe the configuration of magnetic dipole moments, \mathbf{m}_i , in a unit cell which includes two kagome planes and six dipole moments, $i = 1, \dots, 6$. The relative positions of the sublattices from the center of the unit cell are

$$\begin{aligned}
 \Delta\mathbf{r}_1 &= (\Delta x_1, \Delta y_1, \Delta z_1) = a_0 \left(\frac{\sqrt{3}}{6}, -\frac{1}{2}, -\frac{\sqrt{6}}{6} \right) \\
 \Delta\mathbf{r}_2 &= (\Delta x_2, \Delta y_2, \Delta z_2) = a_0 \left(-\frac{\sqrt{3}}{3}, 0, -\frac{\sqrt{6}}{6} \right) \\
 \Delta\mathbf{r}_3 &= (\Delta x_3, \Delta y_3, \Delta z_3) = a_0 \left(\frac{\sqrt{3}}{6}, \frac{1}{2}, -\frac{\sqrt{6}}{6} \right) \\
 \Delta\mathbf{r}_4 &= (\Delta x_4, \Delta y_4, \Delta z_4) = a_0 \left(-\frac{\sqrt{3}}{6}, \frac{1}{2}, \frac{\sqrt{6}}{6} \right) \\
 \Delta\mathbf{r}_5 &= (\Delta x_5, \Delta y_5, \Delta z_5) = a_0 \left(\frac{\sqrt{3}}{3}, 0, \frac{\sqrt{6}}{6} \right) \\
 \Delta\mathbf{r}_6 &= (\Delta x_6, \Delta y_6, \Delta z_6) = a_0 \left(-\frac{\sqrt{3}}{6}, -\frac{1}{2}, \frac{\sqrt{6}}{6} \right),
 \end{aligned} \tag{S1}$$

where $a_0 \approx 0.283$ nm is a distance between Mn atoms.

In the Mn_3Sn case, the magnetic dipole moments at ground state largely have anti-chiral triangular structure at 120° angles to one another, and the dipole moments are confined in the kagome plane [1]. However, the dipole moments slightly rotate from the 120° angle due to the local anisotropy as $\delta\varphi_{i,0}$ which generates a net magnetization of the octupole vector, M_{oct} . The magnetic configuration, $\mathbf{m}_i = (\sin \theta_i \cos \varphi_i, \sin \theta_i \sin \varphi_i, \cos \theta_i)$, at ground state can be describe based on the octupole vector, $\mathbf{m}_{\text{oct}} = (\sin \theta_{\text{oct}} \cos \varphi_{\text{oct}}, \sin \theta_{\text{oct}} \sin \varphi_{\text{oct}}, \cos \theta_{\text{oct}})$, as

$$\begin{aligned}
 \varphi_1 &= \pi - \varphi_{\text{oct}} - \frac{2\pi}{3} + \delta\varphi_{1,0} \\
 \varphi_2 &= \pi - \varphi_{\text{oct}} + \delta\varphi_{2,0} \\
 \varphi_3 &= \pi - \varphi_{\text{oct}} + \frac{2\pi}{3} + \delta\varphi_{3,0} \\
 \varphi_4 &= \pi - \varphi_{\text{oct}} - \frac{2\pi}{3} + \delta\varphi_{4,0} \\
 \varphi_5 &= \pi - \varphi_{\text{oct}} + \delta\varphi_{5,0} \\
 \varphi_6 &= \pi - \varphi_{\text{oct}} + \frac{2\pi}{3} + \delta\varphi_{6,0},
 \end{aligned} \tag{S2}$$

and

$$\theta_1 = \theta_2 = \theta_3 = \theta_4 = \theta_5 = \theta_6 = \theta_{\text{oct}} = \frac{\pi}{2}. \tag{S3}$$

Let us consider a small volume V_c containing $N_{\text{u.c.}}$ unit cells, where \mathbf{m}_{oct} is approximately uniform across the volume. Within this volume, a representative octupole vector, $\mathbf{M}_{\text{oct}} = (\sin \Theta_{\text{oct}} \cos \Phi_{\text{oct}}, \sin \Theta_{\text{oct}} \sin \Phi_{\text{oct}}, \cos \Theta_{\text{oct}})$, can be obtained by averaging \mathbf{m}_{oct} over the volume. The Lagrangian and the dissipative function densities for \mathbf{M}_{oct} can be calculated from Eqs. S2 and S3 as

$$\begin{aligned} L &= N_{\text{u.c.}} \sum_{i=1}^n \left\{ \frac{m_s}{\gamma} \dot{\varphi}_i \cos \theta_i - \epsilon_i \right\} \approx -N_{\text{u.c.}} \sum_{i=1}^n \epsilon_i \quad \text{and} \\ F &= N_{\text{u.c.}} \sum_{i=1}^n \left\{ \alpha \frac{m_s}{2\gamma} (\dot{\theta}_i^2 + \dot{\varphi}_i^2 \sin^2 \theta_i) + j_{\text{hm}} \frac{\theta_{\text{sh}} \hbar}{2ed} \mathbf{p} \cdot (\mathbf{m}_i \times \dot{\mathbf{m}}_i) \right\} \\ &\approx N_{\text{u.c.}} \alpha \frac{\mu_s}{2\gamma} \sum_{i=1}^n \dot{\varphi}_i^2 + N_{\text{u.c.}} \sum_{i=1}^n \left\{ j_{\text{hm}} \frac{\theta_{\text{sh}} \hbar}{2ed} \mathbf{p} \cdot (\mathbf{m}_i \times \dot{\mathbf{m}}_i) \right\}, \end{aligned} \quad (\text{S4})$$

by ignoring small tilt of magnetic moments. In the main text, we show that the small deviation almost does not affect the octupole dynamics by comparing with the results from an atomistic-spin model. Using Eq. S4, we solve the Euler-Lagrangian equation,

$$\begin{aligned} \frac{d}{dt} \frac{\partial L}{\partial \dot{\Theta}_{\text{oct}}} - \frac{\partial L}{\partial \Theta_{\text{oct}}} + \frac{\partial F}{\partial \Theta_{\text{oct}}} &= 0 \quad \text{and} \\ \frac{d}{dt} \frac{\partial L}{\partial \dot{\Phi}_{\text{oct}}} - \frac{\partial L}{\partial \Phi_{\text{oct}}} + \frac{\partial F}{\partial \Phi_{\text{oct}}} &= 0, \end{aligned} \quad (\text{S5})$$

then obtain the equation of motion of Θ_{oct} and Φ_{oct} as

$$\begin{aligned} \dot{\Theta}_{\text{oct}} &= 0 \quad \text{and} \\ \dot{\Phi}_{\text{oct}} &= -\frac{\gamma}{\alpha M_{\text{Mn}} V_c} \frac{\partial E_{\text{tot}}}{\partial \Phi_{\text{oct}}} - \frac{\gamma \theta_{\text{sh}} p_z \hbar}{\alpha 2 M_{\text{Mn}} ed} j_{\text{hm}}, \end{aligned} \quad (\text{S6})$$

respectively. Φ_{oct} is the average of φ_{oct} over the volume, and M_{Mn} is the magnetization of Mn in the unit cell. Note that Eq. S6 is fundamentally identical with the equation of motion of a single octupole moment of a magnetic unit cell reported previously [2, 3].

ANALYTICAL VALUES OF THE OCTUPOLE MAGNETIZATION AND THE SIX-FOLD MAGNETIC ANISOTROPY

The octupole magnetization, \mathbf{M}_{oct} , and the six-fold magnetic energy barrier, K_6 , can be calculated analytically,

$$\begin{aligned} \mathbf{M}_{\text{oct}} &= -\frac{1}{V_{\text{u.c.}}} \frac{m_s K}{J_1 + J_2} \\ K_6 &= \frac{1}{V_{\text{u.c.}}} \frac{K^3}{6(J_1 + J_2)^2}, \end{aligned} \quad (\text{S7})$$

respectively, where $V_{\text{u.c.}}$ is a volume of a magnetic unit cell which contains six magnetic dipole moments. J_1 and J_2 are isotropic exchange interaction constants between inter-plane and intra-plane nearest neighbor moments. $\mathbf{D} = D\hat{\mathbf{z}}$ is an out-of-kagome-plane Dzyaloshinskii-Moriya vector, and K is the single-ion anisotropy constant. Using parameters of Mn_3Sn used in this work, $J_1 = J_2 = -2.803$ meV, $D = -0.635$ meV, $K = 0.187$ meV, and $m_s = 3\mu_B$, we obtained the values from Eq. S7, $\mathbf{M}_{\text{oct}} = 7.2 \text{ kAm}^{-1}$ and $K_6 = 43.3 \text{ Jm}^3$. While these values differ slightly from the numerically obtained values, $\mathbf{M}_{\text{oct}} = 6.1 \text{ kAm}^{-1}$ and $K_6 = 37.5 \text{ Jm}^3$, they are of the same order of magnitude. In our study, we use the numerically obtained values, however, the main results remain unaffected by the choice.

MICROMAGNETIC EXCHANGE ENERGIES

In an Mn_3Sn unit cell, there are six sublattices, i . Their positions, Δr_i , are defined in Eq. S1, and the corresponding magnetic moments, \mathbf{m}_i , can be expressed using Eqs. S2 and S3 at ground state. The unit cell has twelve internal connections and twenty-four connections with the adjacent unit cells, considering only the nearest exchange interactions.

Let us consider the unit cell in a gradually varying non-uniform octupole configuration. Since the magnetic dipole and octupole vectors mostly lie in the kagome plane, the changes of the octupole moments can be described by the variations in the azimuthal angle, $\nabla\varphi_{\text{oct}} = (\partial\varphi_{\text{oct}}/\partial x, \partial\varphi_{\text{oct}}/\partial y, \partial\varphi_{\text{oct}}/\partial z)$. Interestingly, the non-uniformity introduces an additional change of φ_i from the ground state. We assume that $\nabla\varphi_{\text{oct}}$ is sufficiently slow in space, thus the azimuthal angle of the dipole moments in a non-uniform state, $\varphi_{i,\text{nu}}$, can be expressed by

$$\varphi_{i,\text{nu}} = \varphi_i - \nabla\varphi_{\text{oct}} \cdot \Delta r_i. \quad (\text{S8})$$

We calculate an exchange energy in a small volume V_c containing $N_{\text{u.c.}}$ unit cells,

$$N_{\text{u.c.}} = \frac{V_c}{4\sqrt{2}a_0^3}, \quad (\text{S9})$$

where a_0 is a distance between sublattices. Let us assume that the octupole changes only in the x -direction, i.e., $\partial\varphi_{\text{oct}}/\partial x \neq 0$, while $\partial\varphi_{\text{oct}}/\partial y = 0$, and $\partial\varphi_{\text{oct}}/\partial z = 0$. Additionally, we assume that $\partial\varphi_{\text{oct}}/\partial x$ is constant across V_c , so $\partial\Phi_{\text{oct}}/\partial x = \partial\varphi_{\text{oct}}/\partial x$, where Φ_{oct} is an azimuthal angle of octupole magnetization of V_c . In this case, the exchange energy in V_c can be calculated from

Eqs. S1, S2, and S8 as

$$\begin{aligned}
E_{\text{ex},x} = & 4N_{\text{u.c.}}J_1 \cos\left(\frac{\partial\Phi_{\text{oct}}}{\partial x} \frac{1}{2\sqrt{3}}a_0\right) + 2N_{\text{u.c.}}J_1 \cos\left(\frac{\partial\Phi_{\text{oct}}}{\partial x} \frac{1}{\sqrt{3}}a_0\right) + 4N_{\text{u.c.}}J_2 \cos\left(\frac{\partial\Phi_{\text{oct}}}{\partial x} \frac{\sqrt{3}}{2}a_0\right) \\
& + 4N_{\text{u.c.}}\sqrt{3}D \cos\left(\frac{\partial\Phi_{\text{oct}}}{\partial x} \frac{\sqrt{3}}{2}a_0\right)
\end{aligned} \tag{S10}$$

If $\partial\Phi_{\text{oct}}/\partial x$ is sufficiently small, we can rephrase Eq. S10 as

$$\begin{aligned}
E_{\text{ex},x} = & E_{\text{ex},x0} - \left(\frac{J_1}{8\sqrt{2}a_0} + \frac{3J_2}{8\sqrt{2}a_0} + \frac{3D\sqrt{3}}{8\sqrt{2}a_0}\right) \left(\frac{\partial\Phi_{\text{oct}}}{\partial x}\right)^2 V_c \\
= & E_{\text{ex},x0} - A_{\text{ex},x} \left(\frac{\partial\Phi_{\text{oct}}}{\partial x}\right)^2 V_c,
\end{aligned} \tag{S11}$$

where $E_{\text{ex},x0}$ is an x -directional exchange energy in the uniform state. Similarly, we can calculate the exchange stiffness in the y - and z -directions using the same approach, expressed as

$$\begin{aligned}
A_{\text{ex},y} = & -\left(\frac{J_1}{8\sqrt{2}a_0} + \frac{3J_2}{8\sqrt{2}a_0} + \frac{3D\sqrt{3}}{8\sqrt{2}a_0}\right) \quad \text{and} \\
A_{\text{ex},y} = & -\frac{J_1}{2\sqrt{2}a_0},
\end{aligned} \tag{S12}$$

respectively.

ANALYTIC FORM OF A 60-DEGREE DOMAIN WALL PROFILE

We calculate the 60° domain-wall profile. Similar to ferromagnets, the one-dimensional profile has arctan form as

$$\Phi_{\text{oct}}(r) = \frac{1}{3} \arctan\left\{\sinh\left(\frac{\pi r}{\delta}\right)\right\}, \tag{S13}$$

where δ is the width of the domain wall. The optimized δ at the ground state can be obtained when $\partial\Phi_{\text{oct}}/\partial x = 0$, and the domain-wall width can be expressed as

$$\delta_0 = \frac{\pi\sqrt{A}}{3\sqrt{K_6}}, \tag{S14}$$

where A ($= A_x, A_y, A_z$) is an exchange stiffness in the domain-wall propagation direction and K_6 is a six-fold anisotropy constant. In Fig.X, we compare the domain-wall profiles obtained from the micromagnetic simulations and analytical calculation from Eqs. S13 and S14.

[1] M.-T. Suzuki, T. Koretsune, M. Ochi, and R. Arita, *Physical Review B* **95**, 094406 (2017).

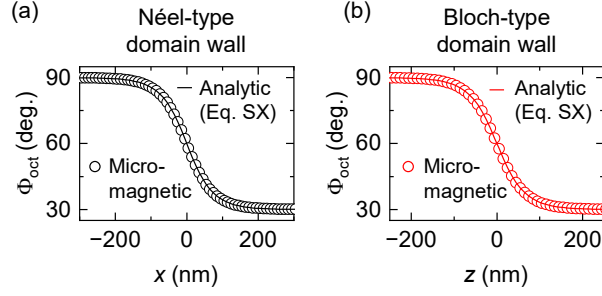


FIG. S1 | (a) Néel-type 60° domain-wall profiles calculated from the micromagnetic simulation (symbols) and the analytic calculation from Eqs. S13 and S14 with $A_{\text{ex},x}$ (line). (b) Same as (a), but for the Bloch-type domain wall with $A_{\text{ex},z}$.

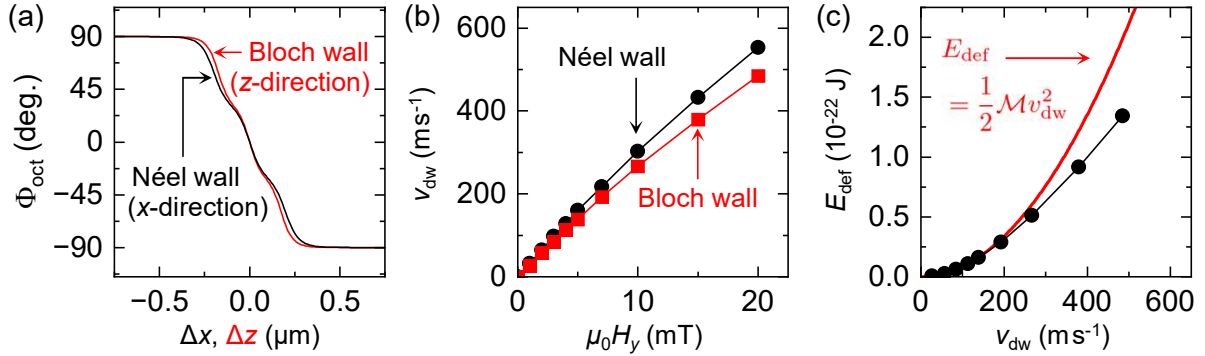


FIG. S2 | Comparison between the 180° Néel- and Bloch-type domain walls in Mn_3Sn . (a) Profiles of the Néel- (black line) and the Bloch-type domain walls in the x - and z -directions, respectively. (b) Domain-wall velocity, v_{dw} , of the Néel- (Black circle) and Bloch-type domain walls (red square) as a function of y -directional magnetic-field strength, H_y . (c) Domain-wall deformation energy, E_{def} , as a function of the Bloch-type domain-wall velocity, v_{dw} (black circle and line). The red line shows a quadratic fit for low v_{dw} . \mathcal{M} is the effective inertial mass of the domain wall for low v_{dw} . The obtained effective inertial mass is $\mathcal{M} \approx 1.7 \times 10^{-27}$ kg.

[2] J. Liu and L. Balents, *Physical Review Letters* **119**, 087202 (2017).

[3] J.-Y. Yoon, P. Zhang, C.-T. Chou, Y. Takeuchi, T. Uchimura, J. T. Hou, J. Han, S. Kanai, H. Ohno, S. Fukami, and L. Liu, *Nature Materials* [10.1038/s41563-023-01620-2](https://doi.org/10.1038/s41563-023-01620-2) (2023).

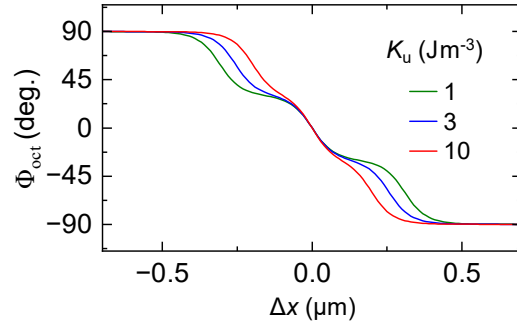


FIG. S3 | Profiles of 180° Néel-type domain walls for different uniaxial anisotropy, $K_u = 1, 3,$ and 10 Jm^{-3} . The domain-wall width decreases with increasing K_u .

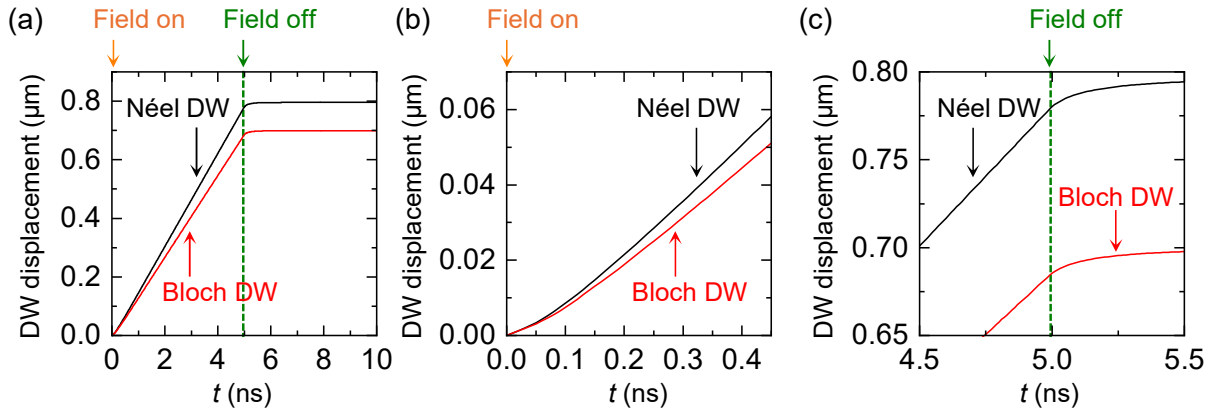


FIG. S4 | Inertial motion of 180° domain walls in Mn_3Sn . (a) Time evolution of the domain-wall (DW) displacement under $+y$ -directional magnetic field, $H_y = 5 \text{ mT}$. The field is turned on and off at 0 and 5 ns , respectively. The black and red lines indicate the Néel- (black line) and the Bloch-type domain walls, respectively. (b) and (c) Magnified view of (a) around $t = 0$ and 5 ns , respectively, to emphasize the inertial dynamics.